

Acoustic Emission Data Based Deep Learning Approach for Classification and Detection of Damage-sources in a Composite Panel

Shirsendu Sikdar^{*,1}, Dianzi Liu² and Abhishek Kundu³

¹Mechanics of Materials and Structures, Department of Materials, Textiles and Chemical Engineering, Ghent University, Technologiepark-Zwijnaarde 46, 9052 Zwijnaarde, Belgium.

^{1,2}Engineering Division, Faculty of Science, University of East Anglia, Norwich, UK.

³Cardiff School of Engineering, Cardiff University, The Parade, Queen's Building, Cardiff, CF24 3AA, UK.

*Corresponding Author: Shirsendu.Sikdar@UGent.be

Abstract

Structural health monitoring for lightweight complex composite structures is being investigated in this paper with a data-driven deep learning approach to facilitate automated learning of the map of transformed signal features to damage classes. Towards this, a series of acoustic emission (AE) based laboratory experiments have been carried out on a composite sample using a piezoelectric AE sensor network. The registered time-domain AE signals from the assigned sensor networks on the composite panel are processed with the continuous wavelet transform to extract time-frequency scalograms. A convolutional neural network based deep learning architecture is proposed to automatically extract the discrete damage features from the scalogram images and use them to classify damage-source regions in the composite panel. The proposed deep-learning approach has shown an effective damage monitoring potential with high training, validation and test accuracy for unseen datasets as well as for entirely new neighboring damage datasets. Further, the proposed network is trained, validated and tested only for the peak-signal data extracted from the raw AE data. The application of peak-signal scalogram data has shown a significant improvement in damage-source classification performance with high training, validation and test accuracy.

Keywords: acoustic emission; composite structure; deep learning; structural health monitoring

1. Introduction

The application of carbon-fiber reinforced composites for lightweight construction is popular in various industrial sectors such as aerospace, automotive, infrastructure and marine engineering [1-2]. Composite structures combine highly desirable properties of high strength-to-weight ratios, acoustic damping, fire resistance and energy-absorption capacity. However, variable operational and loading conditions like- hazardous ambient conditions, impact, cyclic-loading and ageing may lead to the occurrence of damage which can significantly jeopardize the safety of the structural system [2-5]. Assessment of such damage initiation/propagation in these structures under safety-critical engineering applications is of urgent necessity.

Acoustic emission (AE)-based structural health monitoring (SHM) methods are proposed by many authors for damage-source localization in composites [6–11]. In these methods, the sensors record the AE signals that follow damage initiation or the existing damage propagation events within the materials and transforms them into electric waveforms. The study of these AE waveforms can help in understanding the damage characteristics. The AE technique has the capacity for global monitoring without any external excitation [12-13]. Various types of damage sources (pencil lead-break, impact, fatigue) are used as artificial AE-source by the researchers [14-16]. The pencil lead-break (PLB) is popularly adopted as the reproducible artificial AE-source for laboratory-based experiments. However, these studies are mainly focused on damage localisation in composites and there is a need to develop advanced SHM methods for automatic characterisation of such damage-source in composite structures.

In the present era, researchers are focused on developing automated monitoring techniques using experimentally measured structural responses [17-19]. Among those techniques, image-based SHM has shown potential for rapid inspection [20-23]. Nevertheless, the structural damage identification algorithms using the measured data was found to be complicated owing to the influence of pre-defined damage features on the identification results. To avoid such anomaly, deep learning based image classification techniques are adopted which trains the network using the features of the training data set [18,24]. The Convolutional Neural Network (CNN) based deep learning algorithms have proven their potential in image classification [24-27]. The advantage of CNN is its capacity to deal with grid-like inputs, such as images and it produces similar values of features from local regions of similar patterns. Delamination in composites was identified using CNN-based vibration data [28]. Some more applications of CNN in the SHM domain includes the

identification of- cracks in concrete, road cracks, pavement distress, cracks in historical structures, amongst others [29-36]. From the review of literature, it is revealed that image-based deep learning requires a large number of datasets and such a large number of datasets can be synthetically generated by adding a different level of zero-mean Gaussian noise (known as ‘data augmentation’) [37-38]. It is also noticed that there is a lack of work in the area of AE based deep learning for automatic damage-source detection and classification in composite structures, which this paper proposes to address.

This paper proposes a CNN-based deep learning framework for damage-source characterization in a carbon-fiber reinforced composite panel (CFRCP) using AE signals. In the process, a series of laboratory experiments of PLB induced AE in a CFRCP have been carried out using a network of AE sensors. The registered AE signals (time-domain) from experiments are then converted to time-frequency scalograms by performing continuous wavelet transform (CWT) and these scalogram images are used as inputs to the designed CNN architecture for training, validation and testing.

2. Experimental procedure

A CFRCP sample (500 mm × 500 mm × 7 mm) is selected for the laboratory experiment, as shown in Fig. 1. The composite specimen was manufactured from unidirectional pre-preg using a ((0, 90)4)s layup with a vacuum bag. Damage localization has been traditionally performed with approaches considering extracted signal features like arrival time differences. But in practical applications, a zone-based identification of damage sources on the panel can be a robust approach. Here, the focus is on a zone-based assessment of damage sources using acoustic emission signal features. This will also provide a useful confidence measure on the identified locations. The uncertainty in identification is thus ascertained especially in cases where damage is almost equidistant from multiple zones leading to weaker association with a particular class.

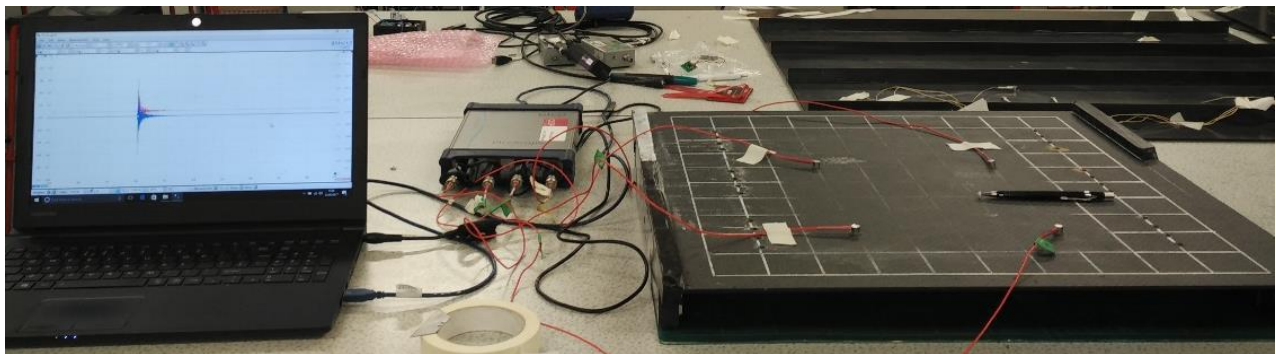


Fig. 1: Experimental setup for PLB damage-induced acoustic emission in the composite panel.

In the sample panel, 5-damage region classes (namely, C1, C2, C3, C4 and C5) are considered as per the proposed PLB source locations, as schematically represented in Fig. 2. In the experiment, 6 mm diameter cylindrical piezoelectric AE sensors are used for the reception of propagating AE signals in the composite panel. The experimental setup consists of a multi-channel AE data-acquisition (ADAQ) system, ‘PicoScope’ for real-time artificial damage-induced AE data reception, a computer to control the DAQ-system and to save the required sensor data (Fig. 1). The PLB source was generated by breaking 0.5 mm dia. 5 mm long pencil leads at a 45° angle (maintained by using a circular support around the pencil). It is worthwhile to note that the differences in handling of the mechanical pencil and the lead diameter can influence the test signals. Also, there is a possibility of simulating the acoustic emission from different types of damage (delamination, matrix crack, fiber breakage) using the PLB test for different modes as discussed in [39]. In the study, a uniformity in lead-breaking angle with sample surface, lead diameter and length were maintained to mitigate such influences. Each of the PLB induced AE events are registered at the assigned sensor network comprised of 8-different sensors marked with S1, S2, S3, S4, S5, S6, S7 and S8 as shown in Fig. 2. Experiments are repeated multiple times for all the cases to collect a large dataset.

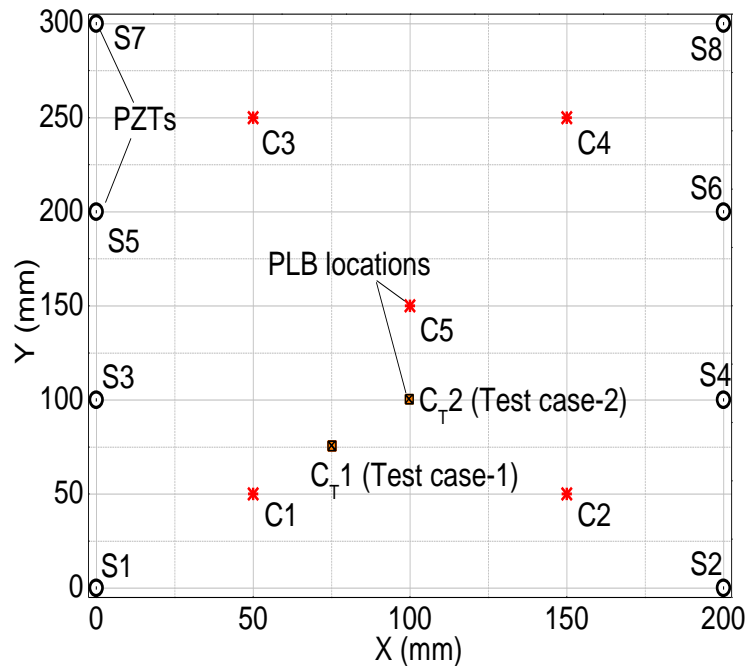


Fig. 2: Schema of the composite panel with pencil lead break positions.

3. SHM strategy for CNN-based damage-source characterization

The proposed SHM strategy directly uses the acquired time-history data from the AE-sensor networks and convert them to time-frequency scalograms by performing CWT considering the Morse Wavelet in MATLAB. These scalogram images are then used as inputs to CNN based deep-learning algorithm, which is trained with the input image datasets to classify the damage-source locations for 5-damage zone classes, C1, C2, C3, C4, and C5. Fig. 3 shows a schematic of the deep learning-based damage classification approach for the current problem. The details of the CNN-based classifier, interpretation of the training and validation process and testing of the pre-trained network are discussed later.

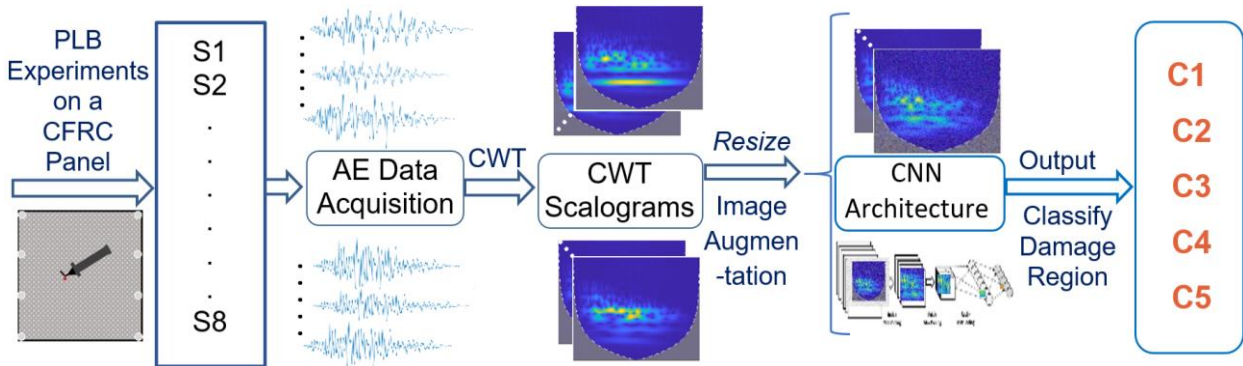


Fig. 3. Schema of the deep learning-based damage assessment in the composite panel.

4. Results and discussion

The experimental AE signals (in time-domain) are obtained from all the 8-sensors for different PLB locations. The registered AE signals at different sensor locations for a typical PLB case (C5) are presented in Fig. 4. The AE data set consisted of a total of 7-cases: 5 training, validation and testing datasets from classes, C1, ..., C5 and 2 additional test datasets from new damage sources, C_{T1} and C_{T2}. In each case, AE signals from 8-AE sensors are obtained.

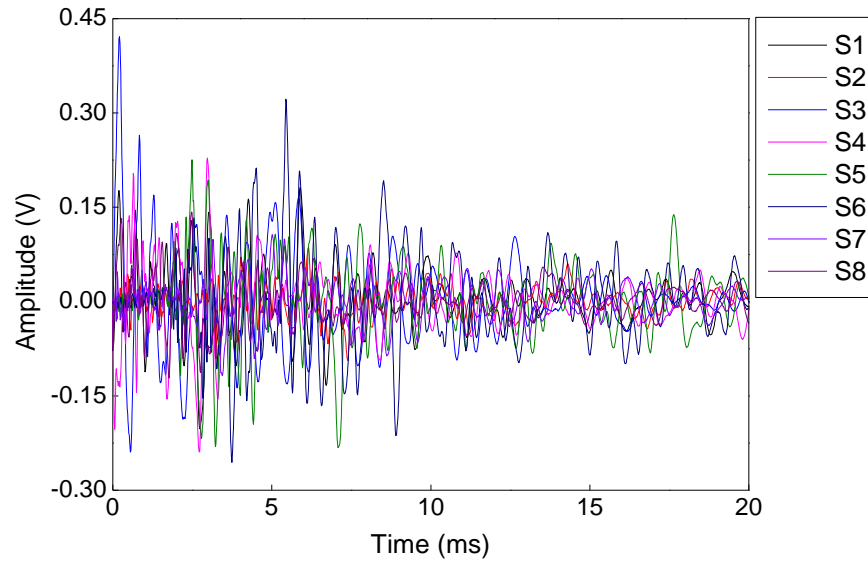


Fig. 4. Raw acoustic emission signals corresponding to the pencil lead break at C5 (ref. Fig 2).

This time-history of AE data are then converted to time-frequency scalogram images by performing CWT in MATLAB, as shown in Fig. 5. It is observed that the sizes of each image data are $[840 \times 630 \times 3]$ (length \times width \times number of channels). In order to reduce computational effort, these images are resized to $[292 \times 219 \times 3]$ pixel using ‘imresize’ in MATLAB. Further, image augmentation is carried out by adding zero-mean Gaussian noise to the reduced scalograms [37-38]. The image resizing and augmentation process is represented in Fig. 5. In the process, 5000 scalogram images are generated and these images are split into 4000 (80%) for training, 500 (10%) for validation and 500 (10%) are used for testing to evaluate the performance of the pre-trained network.

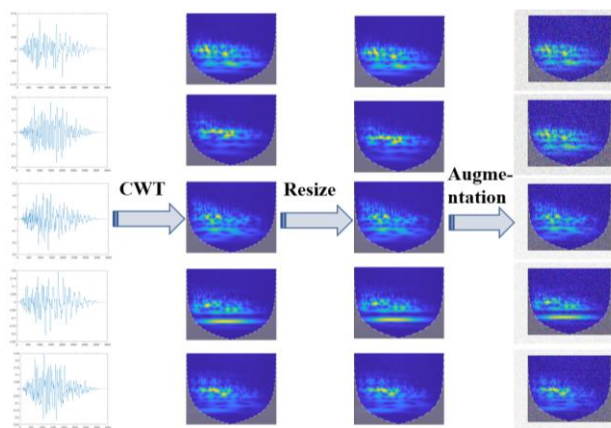


Fig. 5. A typical representation of the scalogram images, resizing the images and image augmentation of S3 signals corresponding to C1, C2, C3, C4 and C5 (ref. Fig 2).

A block diagram of the CNN architecture used for the classification of scalograms is represented in Fig. 6. The proposed CNN architecture shows 6-different layers and the functions of these layers are briefly explained here, however, a detailed description can be found in [40-42]. In the process, the input images are converted to RGB (Red, Green, Blue) pixels [292 × 219 × 3] and forwarded through the network. In the RGB images, each Red, Green and Blue has [292 × 219] pixels. For each matrix, there will be a separate convolution kernel. After convolution, a bias is added. Then the outputs from all 3-channels, are added to obtain the convolution layer output. After the convolution operation, the size of the successive layer reduces that can lead to the loss of information along the border of the generated image feature maps, and to avoid such loss a zero padding is assigned.

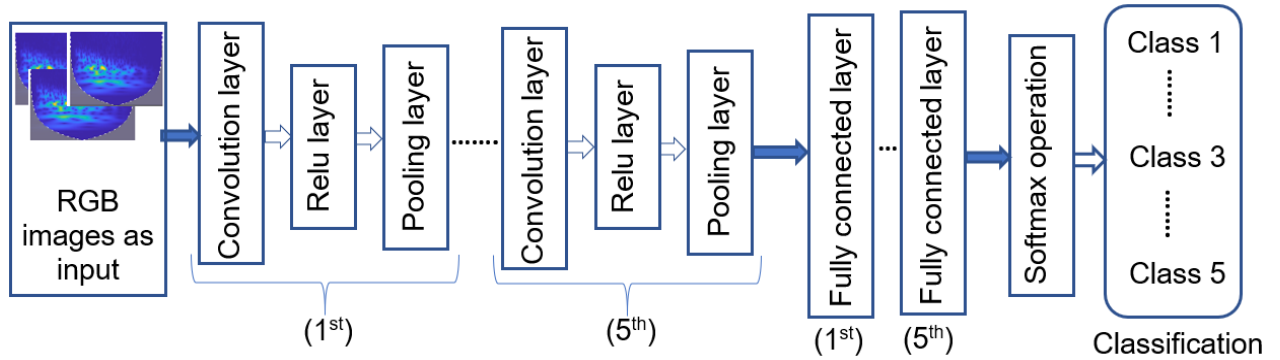


Fig. 6. Convolution neural network architecture used for characterization damage-source regions in the composite panel.

During training, the weights of the convolution kernel and bias are updated by using backpropagation. The size of the convolution kernel (filter) for the present study is 8×8 pixels and the number of kernels used is 20 (based on trials) to take care of the important information. After convolution, a rectified linear unit (RELU) activation function given in Eq. 1 is used to map each negative element value to ‘0’. This RELU activation function is found to be advantageous in terms of speed and accuracy over ‘sigmoid’ and ‘tanh’ function [40].

$$f(x) = \begin{cases} x & x \geq 0 \\ 0 & x < 0 \end{cases} \quad 1$$

After RELU, the pooling layer (Fig. 6) performs a down-sampling operation that reduces the dimensionality of the feature maps. In the study, the pooling operation is done by max-pooling that picks the maximum value of the sliding window of size [2 × 2]. The classification phase starts from the fully connected layer, which takes the output of the last pooling layer as input. In the process, the neurons in the previous layer remain connected to the neurons in the fully connected

layer. To identify the larger patterns, all the features learned by the previous layer are combined in this layer. A fully connected layer multiplies the input by a weight matrix [a] and then adds a bias vector. In this study, the output size of the fully connected layer of the network is equal to the number of dataset classes (i.e. 5).

Training of this deep learning network is a stochastic gradient descent with momentum (SGDM) based optimization process that minimizes the loss for the given training dataset by updating weights. This optimization process computes the gradient of the loss function at each iteration step. The input vectors of the loss function are image pixel, bias and weight. In the study, the *softmax* function with multinomial logistic loss is considered as the loss function [42-43]. The *Softmax* is a neural transfer function that calculate a layer's output from its net input [43]. For a given feature sample x and its true class N_i , the posterior probability (P_i) is represented as:

$$y_i = P_i(N_i|x) = \frac{\exp[a_i^T x + a_{i0}]}{\sum_{j=1}^k \exp[a_j^T x + a_{j0}]} \quad 2$$

where $y(y_1, y_2, \dots, y_c)$ is the score vector that calculates the output vectors with elements between 0 and 1, but with their size relations intact, a_0 and a_i are the bias and weights updated by backpropagation, and 'T' stands for the transpose operation. The loss function is defined as:

$$L(A) = -Y_g^T \ln(y) \quad 3$$

where the ground-truth vector, $Y_g(Y_{g1}, Y_{g2}, \dots, Y_{gc})$ and y formulate the loss function that estimates the distance between the present model and the targeted model. The ground truth function value is one for the targeted neuron and zero for the other neurons. The loss function is minimised by updating the bias and weights. The updated weights are calculated as:

$$a_{new} = a_{old} - \psi \frac{\delta L}{\delta a_{old}} \quad 4$$

where ' ψ ' is the user-defined learning rate based on information accuracy and computational time. In multi-class classification problems, the classification layers estimate the cross-entropy loss, ε with N mutually exclusive classes. A *softmax* layer and then a classification layer must follow the final fully connected layer. For multi-class classification problems, it assigns data to one of the N mutually exclusive classes. The loss function for this case is the cross-entropy function for a *1-of-N* coding scheme. In this classification algorithm, the logarithmic loss (cross-entropy loss) is calculated as:

$$\varepsilon = -\frac{1}{S} \sum_{i=1}^S \sum_{j=1}^N y_{ij} \cdot \log q_{ij} \quad 5$$

where S represents the number of samples, N represents the number of classes, q_{ij} is either one indicating whether the sample number i belongs to the class number j else zero, and k_{ij} represents the output for sample i and class j obtained from the *softmax* function [40,42].

The proposed deep learning network (Fig. 6) is trained, validated and tested with the processed CWT scalogram image inputs. To achieve a stable performance of the network, 10-fold training, validation and testing have been carried out. In the process, 5000 images corresponding to the 5-damage classes (C_1, \dots, C_5) are divided into 10- parts (i.e. 500/part). Stage-1: part#1 (i.e. 10% of 5000 images) for Testing and part#2,3,4,5,6,7,8,9,10 for Training (90% of these 4500 images) and Validation (10% of these 4500 images). Stage-2: part#2 for Testing and Part#1,3,4,5,6,7,8,9,10 for Training and Validation. Similarly, Stage-3 to Stage-10 have been carried out for Training, Validation and Testing of the proposed network.

One of the training-validation results is presented in Fig. 7 shows the averaged courses of validation accuracy and loss. The network is trained for 10-epochs with 31-iterations/epochs without any overfitting occurring. The validation accuracy takes approximately 5 to 6 epochs to converge, which is visible from the decreasing loss curve in Fig. 7.

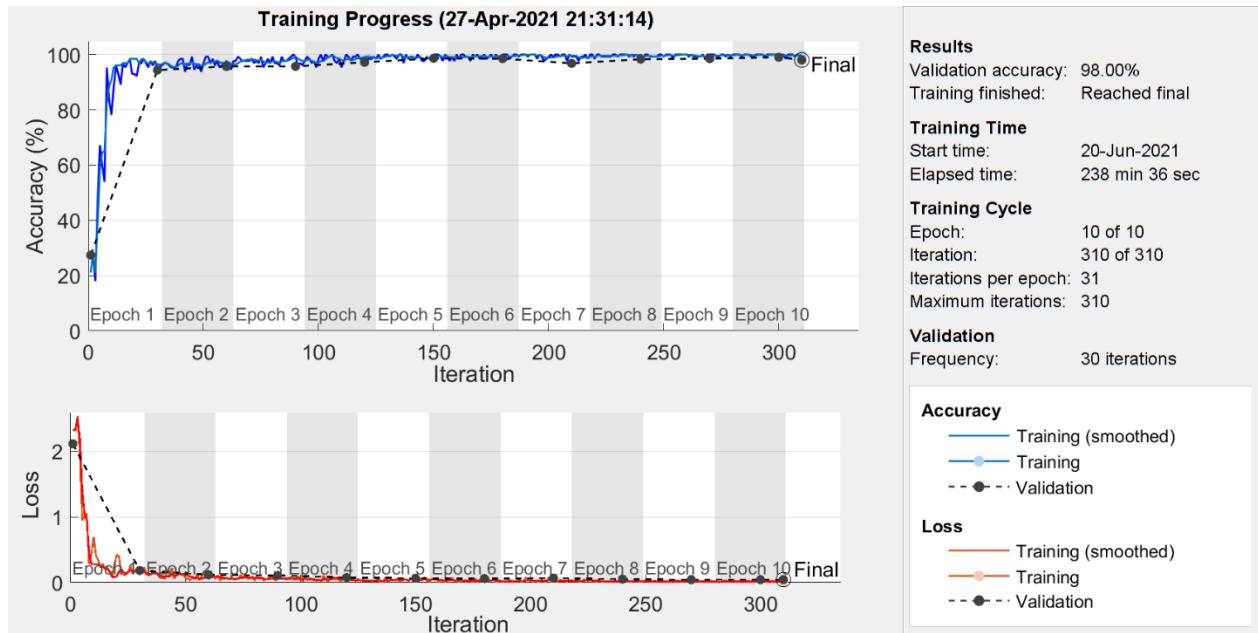


Fig. 7. A typical training-validation curve shows a comparison of the accuracy and loss in training and validation of the network.

The network continuously improves its confidence for an accurate prediction. In early epochs, some oscillations are noticed in validation accuracy and loss curves, owing to the limited data used in a single batch. The weights are updated after the passing batches with a proportion of all possible classes through CNN. The results show that the average 10-fold training/validation Accuracy = $\{(96.8 + 97.5 + 97 + 98 + 97.65 + 97.24 + 96.94 + 97.2 + 98 + 98) / 10\} = 97.36\%$. Table 1 confusion matrix shows the 10-fold average (av.) test accuracy results for each of the damage classes. The test result shows a predictive overall (10-fold av.) test accuracy of 95.48%. The damage-source region classification performance of the proposed deep learning network is also tested for two new damage case C_{T1} (near $C1$) and $CT2$ (close to $C5$) datasets as marked in Fig. 2. During this testing, both C_{T1} and C_{T2} data are supplied from the test dataset channel $C1$ of the network. In Table 2, the 10-fold av. test results for the C_{T1} data, which was supplied as the $C1$ of the network shows an accuracy of 89.4% that indicates the robustness of the proposed deep learning architecture in classifying the most relevant zone of an untrained damage (C_{T1}) in the neighbourhood of a trained damage class (i.e. $C1$).

Table 1. Confusion matrix represents 10-fold av. test performance of the deep learning network.

		Confusion Matrix						
Output Class		C1	C2	C3	C4	C5	Accuracy	Loss
		C1	95.6 19.12%	3.8 0.76%	1.2 0.24%	2.6 0.52%	0.7 0.14%	92.01% 7.99%
C2	2.0 0.4%	94.3 18.86%	2.2 0.44%	0.8 0.16%	0.7 0.14%	94.3% 5.7%		
C3	1.9 0.38%	0 0.0%	96.6 19.32%	0.2 0.04%	0.4 0.08%	97.48% 2.52%		
C4	0.5 0.1%	1.6 0.32%	0 0.0%	95.2 19.04%	0.8 0.16%	97.04% 2.96%		
C5	0 0.0%	0.4 0.08%	0 0.0%	1.2 0.24%	95.7 19.14%	98.35% 1.65%	$95.7 / (100 * 5) = 19.14$	$1.2 / 500 = 0.24$
		95.6% 4.4%	94.3% 5.7%	96.6% 3.4%	95.2% 4.8%	95.7% 4.3%	95.48%	4.52%
		$(0 + 0.5 + 1.9 + 2.0) = 4.4$					$(95.6 + 94.3 + 96.6 + 95.2 + 95.7) / 5 = 95.48$	$(4.4 + 5.7 + 3.4 + 4.8 + 4.3) / 5 = 4.52$
		C_1	C_2	C_3	C_4	C_5		
		Target Class						

Table 2. Confusion matrix of the 10-fold av. test performance of the network for C_{T1} data.

Confusion Matrix

Output Class	C1	89.4 89.4%	0 0.0%	0 0.0%	0 0.0%	0 0.0%	100% 0.0%
	C2	4.2 4.2%	0 0.0%	0 0.0%	0 0.0%	0 0.0%	0.0% 100%
	C3	0 0.0%	0 0.0%	0 0.0%	0 0.0%	0 0.0%	NaN% 100%
	C4	0 0.0%	0 0.0%	0 0.0%	0 0.0%	0 0.0%	NaN% NaN%
	C5	6.4 6.4%	0 0.0%	0 0.0%	0 0.0%	0 0.0%	0.0% 100%
			89.4% 10.6%	NaN% NaN%	NaN% NaN%	NaN% NaN%	NaN% NaN%
		C_1	C_2	C_3	C_4	C_5	
		Target Class					

Whereas, for C_{T2} data (as C_1 input), it shows an interesting test result with 15.3% of C_1 , 19.1% of C_2 , 8.3% of C_3 , 2.4% of C_4 and 54.9% of C_5 data, as given in Table 3. Such distribution of test results is happened due to the variable influence of different trained damage classes (C_1 , C_2 , C_3 , C_4 , C_5) based on their distance from C_{T2} , which is evident from Fig. 2. In the confusion matrix, the NaN% represents no inputs in the C_2 , C_3 , C_4 and C_5 channels of the Target Class and no outputs in C_3 and C_4 channels of the output class.

Table 3. Confusion matrix of the 10-fold av. test performance of the network for C_T2 data.

Confusion Matrix

Output Class	C1	15.3 15.3%	0 0.0%	0 0.0%	0 0.0%	0 0.0%	100% 0.0%
	C2	19.1 19.1%	0 0.0%	0 0.0%	0 0.0%	0 0.0%	0.0% 100%
	C3	8.3 8.3%	0 0.0%	0 0.0%	0 0.0%	0 0.0%	0.0% 100%
	C4	2.4 2.4%	0 0.0%	0 0.0%	0 0.0%	0 0.0%	0.0% 100%
	C5	54.9 54.0%	0 0.0%	0 0.0%	0 0.0%	0 0.0%	0.0% 100%
			15.3% 84.7%	NaN% NaN%	NaN% NaN%	NaN% NaN%	NaN% NaN%
		C ¹	C ²	C ³	C ⁴	C ⁵	
		Target Class					

The AE based damage-source classification study was further extended for a 10-fold training, validation and testing with the filtered peak-signals of the raw AE data (time-domain) registered at 8-sensor locations. These peak-signals are considered for a temporal bandwidth of 2 ms starting from the initiation of the highest- peak in each of the AE responses from S1,..., S8 sensors, as typically represented in Fig. 8 for the PLBD at C5. It is observed that the peak-signal magnitudes vary with the difference in PLB-to-sensor distance and similar signal patterns are observed in all the study cases.

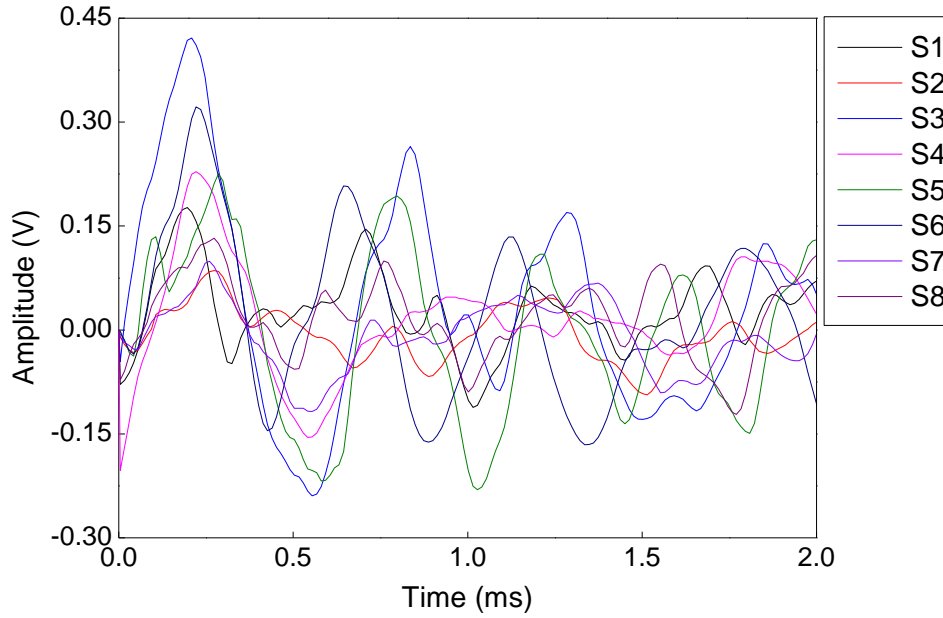


Fig. 8. Extracted peak-signals from the raw AE data registered at sensors S1,..S8 corresponding to pencil lead break at C5 (ref. Fig 2).

The proposed deep learning network (ref. Fig. 6) is again trained, validated and tested with the CWT scalogram images of the peak-signals. Fig. 9 typically represents the time-frequency scalogram images of the peak-signals from S3 corresponding to C1, C2, C3, C4, C5 (ref. Fig 2).

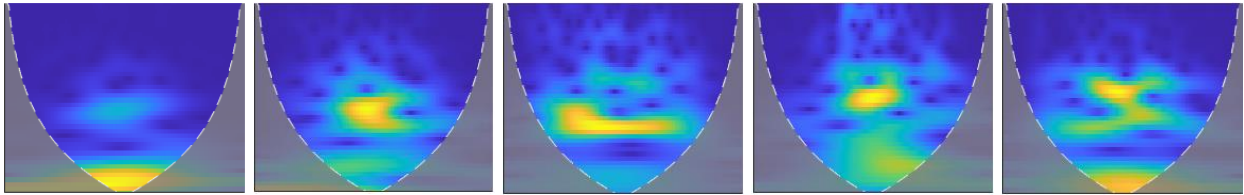


Fig. 9. Scalograms of the peak-signals from S3 data from C1, C2, C3, C4, C5 (ref. Fig 2).

A 10-fold training-validation and testing have been carried out. One of the training-validation results is presented in Fig. 10. The validation accuracy takes approximately 4 to 5 epochs to converge, which is visible from the decreasing loss curve. The results show that the average 10-fold training/validation Accuracy = $\{(98.68 + 98.48 + 99.22 + 99.34 + 99.12 + 98.89 + 99 + 98.7 + 99.11 + 99.17)/10\} = 98.97\%$, which is higher than the result (i.e. 97.36%) obtained for the raw AE signals. Further, a comparison between 10-fold training validation results corresponding to the raw AE signals and peak-signal is presented in Fig. 11. The results show a consistently higher performance for the extracted peak-signal AE data.

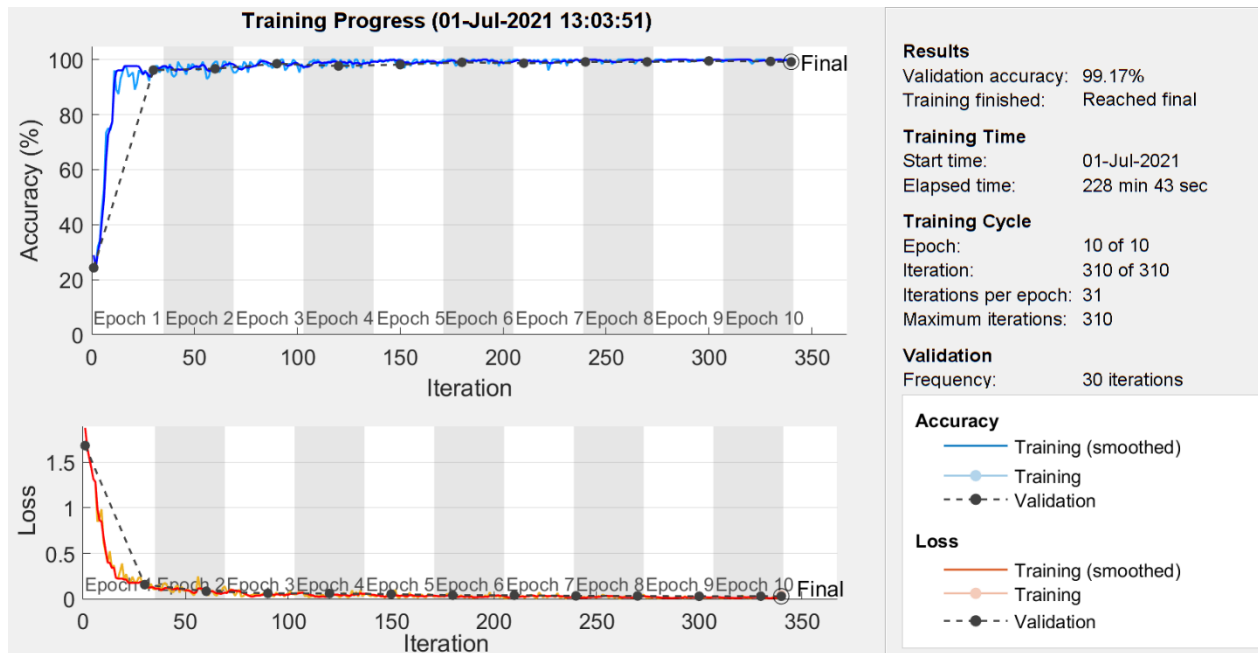


Fig. 10. A typical training-validation result of the proposed network for the peak-signal data.

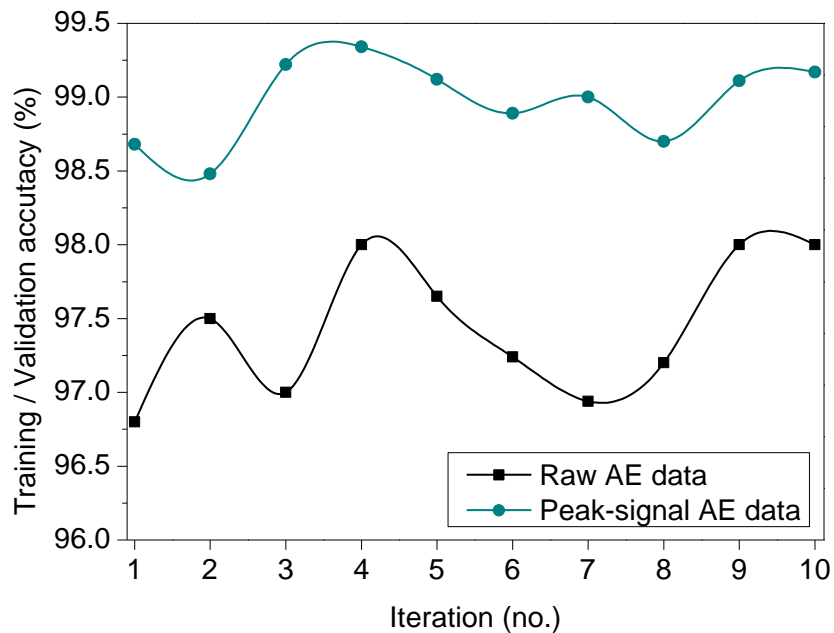


Fig. 11. Comparing 10-fold training-validation accuracy of the network for raw & peak-signal data.

The 10-fold average test (with 100 scalograms/class) results of the trained networks show 96.2% accuracy, as given in Table 4 confusion matrix. The confusion matrix also shows the 10-fold average test accuracy results for each class. Further, a comparison between the 10-fold average test accuracy results (Table 1) corresponding to the raw AE data and the test accuracy results (Table 4)

corresponding to the filtered peak-signal data is presented in Fig. 12 that indicates a significant increase in the peak-signal data results over the raw AE data.

Table 4. Confusion matrix shows 10-fold av. test results of the network with peak-signal data.

Confusion Matrix

Output Class	C1	C2	C3	C4	C5	
C1	95.8 19.12%	2.7 0.54%	0.8 0.16%	1.7 0.34%	0.8 0.16%	94.11% 5.89%
C2	2.2 0.44%	95.5 19.10%	1.7 0.34%	0.7 0.14%	1.0 0.20%	94.46% 5.54%
C3	1.2 0.24%	0 0.0%	97.1 19.42%	0 0.0%	0.8 0.16%	97.98% 2.02%
C4	0.8 0.16%	1.4 0.28%	0 0.0%	96.4 19.28%	1.2 0.24%	96.59% 3.41%
C5	0.0 0.0%	0.4 0.08%	0.4 0.08%	1.2 0.24%	96.2 19.24%	97.96% 2.04%
	95.8% 4.2%	95.5% 4.5%	97.1% 2.9%	96.4% 3.6%	96.2% 3.8%	96.20% 3.80%
	C1	C2	C3	C4	C5	
	Target Class					

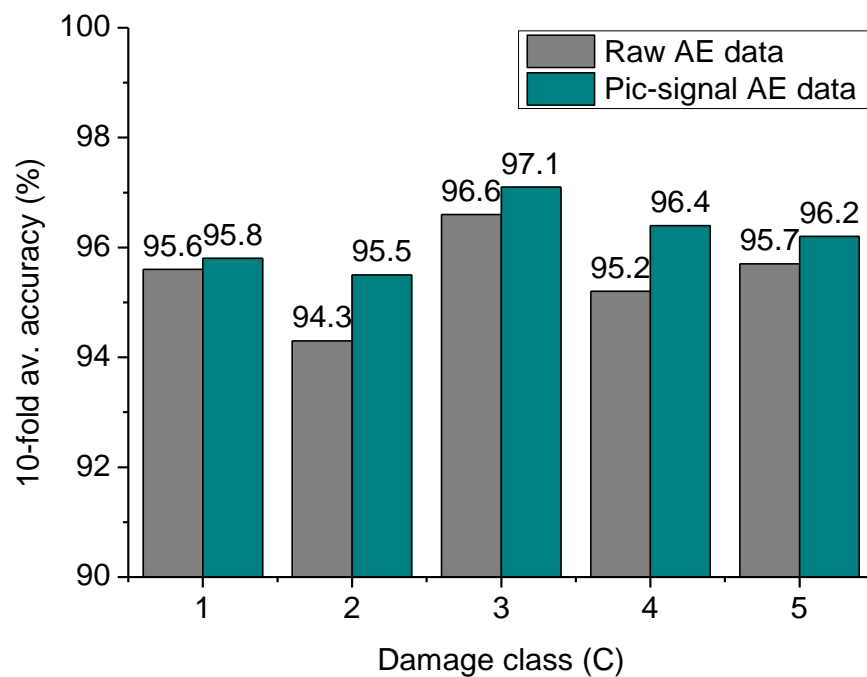


Fig. 12. Comparison of 10-fold av. test accuracy for the raw and the peak-signal AE data.

The damage-source classification performance of the proposed deep learning network is again tested for the peak-signal scalogram datasets from C_{T1} and C_{T2} (ref. Fig. 2). The test results are presented in Table 5 and Table 6 that shows a better performance of the proposed network.

Table 5. Confusion matrix shows test performance for the C_{T1} peak-signal data.

Output Class	C1	C2	C3	C4	C5	
C1	91.6 91.6%	0 0.0%	0 0.0%	0 0.0%	0 0.0%	100% 0.0%
C2	3.4 3.4%	0 0.0%	0 0.0%	0 0.0%	0 0.0%	0.0% 100%
C3	0 0.0%	0 0.0%	0 0.0%	0 0.0%	0 0.0%	NaN% 100%
C4	0 0.0%	0 0.0%	0 0.0%	0 0.0%	0 0.0%	NaN% NaN%
C5	5 5.0%	0 0.0%	0 0.0%	0 0.0%	0 0.0%	0.0% 100%
	91.6% 8.4%	NaN% NaN%	NaN% NaN%	NaN% NaN%	NaN% NaN%	91.6% 8.4%
	C1	C2	C3	C4	C5	
	Target Class					

Table 6. Confusion matrix shows test performance for C_{T2} peak-signal data.

Output Class	C1	C2	C3	C4	C5	
C1	16.2 16.2%	0 0.0%	0 0.0%	0 0.0%	0 0.0%	100% 0.0%
C2	15.3 15.3%	0 0.0%	0 0.0%	0 0.0%	0 0.0%	0.0% 100%
C3	3.8 3.8%	0 0.0%	0 0.0%	0 0.0%	0 0.0%	0.0% 100%
C4	2.2 2.2%	0 0.0%	0 0.0%	0 0.0%	0 0.0%	0.0% 100%
C5	62.5 62.5%	0 0.0%	0 0.0%	0 0.0%	0 0.0%	0.0% 100%
	16.2% 83.8%	NaN% NaN%	NaN% NaN%	NaN% NaN%	NaN% NaN%	16.2% 83.8%
	C1	C2	C3	C4	C5	
	Target Class					

For the given C_{T2} data (as $C1$ input), it shows an interesting result with 16.2% of $C1$, 15.3% of $C2$, 3.8% of $C3$, 2.2% of $C4$ and 62.5% of $C5$ images. This distribution resembles the influence of the trained PLB damage-source classes based on their distance from C_{T2} (ref. Fig. 2). In the confusion matrixes, the NaN% occurs due to the absence of input data in $C2$, $C3$, $C4$ and $C5$ Target Classes. The comparison between the raw and peak-signal image-based 10-fold av. test results for C_{T1} and C_{T2} are compared and presented in Fig. 13(a) and Fig. 13(b), respectively for a better understanding of their effectiveness. The comparison shows a better test accuracy for the extracted peak-signal image data, in both the study cases.

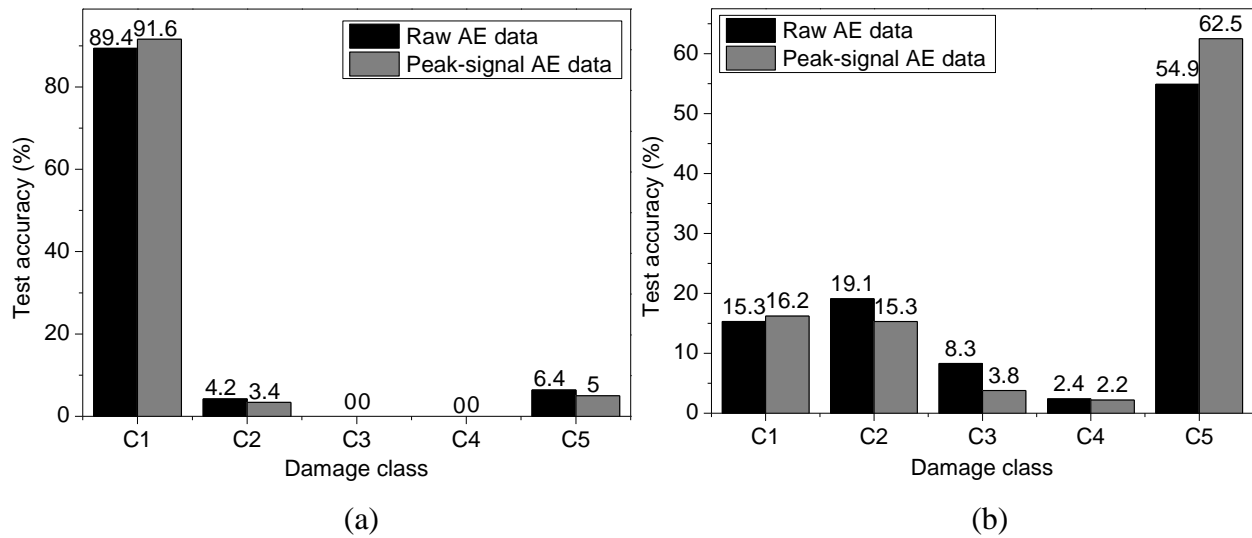


Fig. 13. 10-fold av. test accuracy of (a) C_{T1} and (b) C_{T2} for the raw and their peak-signal data.

5. Conclusions

AE data-based deep learning approach is proposed for automatic damage-source region monitoring in the composite panel. The proposed approach has proven its potential in the effective characterisation of damage-source locations in the targeted composite panel. Moreover, this SHM approach does not require the labour-intensive process of handcrafted discriminative features and directly uses the raw and uncalibrated AE-sensor signals for the local and global assessment of damage in the composite structure.

- The test confusion charts of the pre-trained CNN revealed that the proposed SHM approach can effectively distinguish the 5-primary damage-source classes in the CFRCP with high accuracy using the untrained as well as with entirely new neighbouring damage case datasets.

- The proposed deep network produced better training, validation and test accuracy (10-fold av.) with the extracted peak-signal scalogram data than the raw AE signal scalogram data.
- The comparison between the 10-fold average test accuracy results of raw AE data and the filtered peak-signal data in Fig. 12 shows that the proposed approach is more efficient with the filtered peak-signal images.

It is envisioned that the research will significantly contribute to the SHM research community towards the development of artificial intelligence-based robust industry-grade SHM tools in the future. The future research will involve the characterisation of different damage types in composite structures, especially with regards to

- the sensitivity of differential signal features to damage characteristics, size and severity;
- exploring unsupervised machine learning approaches like hierarchical clustering for classifying damage-related acoustic events and outlier identification
- probabilistic uncertainty quantification to account for effects of variable operational and ambient conditions on identified damage metrics

These comprise the ongoing research by the authors.

Acknowledgement

This research was supported by the Research Foundation-Flanders (FWO) Belgium under grant agreement no. FWO.3E0.2019.0102.01 in the frame of FWO Marie Curie Fellowship. Abhishek Kundu wishes to acknowledge the support from Royal Academy of Engineering, UK for the Industrial Fellowship, reference IF\192013.

References

- [1] Gay D. Composite materials: design and applications. CRC press; 2014 Jul 29.
- [2] Huo X, Luo Q, Li Q, Sun G. Measurement of fracture parameters based upon digital image correlation and virtual crack closure techniques. *Composites Part B: Engineering*. 2021 Jul 18:109157.
- [3] Safri SN, Sultan MT, Jawaid M, Jayakrishna K. Impact behaviour of hybrid composites for structural applications: A review. *Composites Part B: Engineering* 2017;133:112-121.

- [4] Sha G, Radzienski M, Soman R, Cao M, Ostachowicz W, Xu W. Multiple damage detection in laminated composite beams by data fusion of Teager energy operator-wavelet transform mode shapes. *Composite Structures*. 2020 Mar 1;235:111798.
- [5] Chen D, Luo Q, Meng M, Li Q, Sun G. Low velocity impact behavior of interlayer hybrid composite laminates with carbon/glass/basalt fibres. *Composites Part B: Engineering*. 2019 Nov 1;176:107191.
- [6] Green ER. Acoustic emission in composite laminates. *J Nondestr Eval*, 1998;17:117–27.
- [7] Giordano M, Calabro A, Exposito C, D'Amore A, Nicolais L. An acoustic-emission characterization of the failure modes in polymer composite materials. *Compos Sci Technol* 1998;58:1923–8.
- [8] Unnthorsson R, Runarson TP, Jonsson MT. Acoustic emission based failure criterion for CFRP. *Int J Fatig* 2008;30:11–20.
- [9] Sikdar S, Ostachowicz W, Pal J. Damage-induced acoustic emission source identification in an advanced sandwich composite structure. *Composite Structures*. 2018 Oct 15;202:860-6.
- [10] Lissek F, Haeger A, Knoblauch V, Hloch S, Pude F, Kaufeld M. Acoustic emission for interlaminar toughness testing of CFRP: evaluation of the crack growth due to burst analysis. *Compos B Eng* 2018;136:55–62.
- [11] Wevers M, Lambrighs K. Applications of acoustic emission for SHM: a review. *Encyclopedia of structural health monitoring*. John Wiley & Sons; 2009.
- [12] Ono K, Gallego A. Research and application of AE on advanced composite. *J Acoust Emiss* 2012;30:180–229.
- [13] MacIntire P, editor. *Nondestructive testing handbook: acoustic emission testing*. American Society for Nondestructive Testing; 1987.
- [14] Unnthorsson R, Runarson TP, Jonsson MT. Acoustic emission based failure criterion for CFRP. *Int J Fatig* 2008;30:11–20.
- [15] Al-Jumaili SK, Holford KM, Eaton MJ, Pullin R. Parameter Correction Technique (PCT): a novel method for acoustic emission characterisation in large-scale composites. *Compos B Eng* 2015;75:336–44.
- [16] Sikdar S, Mirgal P, Banerjee S, Ostachowicz W. Damage-induced acoustic emission source monitoring in a honeycomb sandwich composite structure. *Composites Part B: Engineering*. 2019 Feb 1;158:179-88.

- [17] Liu F, Gao S, Tian Z, Liu D. A new time-frequency analysis method based on single mode function decomposition for offshore wind turbines. *Marine Structures*. 2020 Jul 1;72:102782.
- [18] Liu H, Zhang Y. Image-driven structural steel damage condition assessment method using deep learning algorithm. *Measurement*. 2019 Feb 1;133:168-81.
- [19] Kundu A, Sikdar S, Eaton M, Navaratne R. A Generic Framework for Application of Machine Learning in Acoustic Emission-Based Damage Identification. In *Proceedings of the 13th International Conference on Damage Assessment of Structures 2020* (pp. 244-262). Springer, Singapore.
- [20] Jia Y, Shelhamer E, Donahue J, Karayev S, Long J, Girshick R, Guadarrama S, Darrell T. Caffe: Convolutional architecture for fast feature embedding. In *Proceedings of the 22nd ACM international conference on Multimedia 2014* Nov 3 (pp. 675-678).
- [21] Sikdar S, Pal J. Bag of Visual Words based Machine Learning Framework for Disbond Characterisation in Composite Sandwich Structures using Guided Waves. *Smart Materials and Structures*. 2021 May 14, 30: p. 075016.
- [22] Jacobsen A, Hitaka T, Nakashima M. Online test of building frame with slit-wall dampers capable of condition assessment. *Journal of Constructional Steel Research*. 2010 Nov 1;66(11):1320-9.
- [23] Chen FC, Jahanshahi MR. NB-CNN: Deep learning-based crack detection using convolutional neural network and Naïve Bayes data fusion. *IEEE Transactions on Industrial Electronics*. 2017 Oct 19;65(5):4392-400.
- [24] Tao C, Zhang C, Ji H, Qiu J. Fatigue damage characterization for composite laminates using deep learning and laser ultrasonic. *Composites Part B: Engineering*. 2021 Jul 1;216:108816.
- [25] Ren S, He K, Girshick R, Sun J. Faster r-cnn: Towards real-time object detection with region proposal networks. In *Advances in neural information processing systems 2015* (pp. 91-99).
- [26] Gonzalez TF, editor. *Handbook of approximation algorithms and metaheuristics*. CRC Press; 2007.
- [27] Kumar SS, Abraham DM, Jahanshahi MR, Iseley T, Starr J. Automated defect classification in sewer closed circuit television inspections using deep convolutional neural networks. *Automation in Construction*. 2018;91:273-83.

- [28] Khan A, Shin JK, Lim WC, Kim NY, Kim HS. A Deep Learning Framework for Vibration-Based Assessment of Delamination in Smart Composite Laminates. *Sensors*. 2020;20(8):2335.
- [29] Alvarez-Montoya J, Carvajal-Castrillón A, Sierra-Pérez J. In-flight and wireless damage detection in a UAV composite wing using fiber optic sensors and strain field pattern recognition. *Mechanical Systems and Signal Processing*. 2020;136:106526.
- [30] Ebrahimkhanlou A, Salamone S. Single-sensor acoustic emission source localization in plate-like structures using deep learning. *Aerospace*. 2018;5(2):50.
- [31] De Oliveira MA, Monteiro AV, Vieira Filho J. A new structural health monitoring strategy based on PZT sensors and convolutional neural network. *Sensors*. 2018;18(9):2955.
- [32] Cha YJ, Choi W, Büyüköztürk O. Deep learning- based crack damage detection using convolutional neural networks. *Computer- Aided Civil and Infrastructure Engineering*. 2017 May;32(5):361-78.
- [33] Fan Z, Wu Y, Lu J, Li W. Automatic pavement crack detection based on structured prediction with the convolutional neural network. *arXiv preprint arXiv:1802.02208*. 2018.
- [34] Zhang L, Yang F, Zhang YD, Zhu YJ. Road crack detection using deep convolutional neural network. In *2016 IEEE international conference on image processing (ICIP) 2016 Sep 25 (pp. 3708-3712)*. IEEE.
- [35] Gopalakrishnan K, Khaitan SK, Choudhary A, Agrawal A. Deep convolutional neural networks with transfer learning for computer vision-based data-driven pavement distress detection. *Construction and Building Materials*. 2017 Dec 30;157:322-30.
- [36] Dorafshan S, Thomas RJ, Maguire M. Comparison of deep convolutional neural networks and edge detectors for image-based crack detection in concrete. *Construction and Building Materials*. 2018 Oct 20;186:1031-45.
- [37] Ewald V, Goby X, Jansen H, Groves RM, Benedictus R. Incorporating Inductive Bias into Deep Learning: A Perspective from Automated Visual Inspection in Aircraft Maintenance. In *Proc. 10th Intl Symposium on NDT in Aerospace, Dresden 2018 (pp. 1-9)*.
- [38] Ewald V, Groves RM, Benedictus R. DeepSHM: a deep learning approach for structural health monitoring based on guided Lamb wave technique. In *Sensors and Smart Structures Technologies for Civil, Mechanical, and Aerospace Systems 2019 2019 Mar 27 (Vol. 10970, p. 109700H)*. International Society for Optics and Photonics.

- [39] Dunegan HL. An alternative to pencil lead breaks for simulation of acoustic emission signal sources. The DECI report. 2000 Aug.
- [40] Kim H, Kim H, Hong YW, Byun H. Detecting construction equipment using a region-based fully convolutional network and transfer learning. *Journal of computing in Civil Engineering*. 2018;32(2):04017082.
- [41] Huang X, Liu Z, Zhang X, Kang J, Zhang M, Guo Y. Surface damage detection for steel wire ropes using deep learning and computer vision techniques. *Measurement*. 2020 Sep 1; 161:107843.
- [42] Yamashita R, Nishio M, Do RK, Togashi K. Convolutional neural networks: an overview and application in radiology. *Insights into imaging*. 2018 Aug 1; 9(4):611-29.
- [43] MATLAB R2021a, Natick, Massachusetts: The MathWorks Inc.; 2021.